An Accurate Device for Apparent Emissivity Characterization in Controlled Atmospheric Conditions Up To 1423 K

Chengxi Zhu, Matthew J. Hobbs, Robert C. Masters, Cornelia Rodenburg, and Jon R. Willmott

***Abstract*—Emissivity is a material property that must be measured before an accurate noncontact temperature measurement can be made. We have developed a novel instrument for measuring apparent emissivity under a controlled atmosphere, providing data for applications in radiation thermometry. Our instrument employs a split furnace, a sample-blackbody component, two custom-designed radiometers, and a controlled atmospheric system. We measure across the temperature range from 973 to 1423 K and the spectral range from 0.85 to 1.1 μm; this range is matched to the majority of high-temperature radiation thermometers. The sample and reference approximate blackbody are heated and maintained in the thermal equilibrium, with a temperature difference of better than 1 K at 1423 K. The combined standard uncertainty of the system is lower than 0.0590 (at $k = 2$) over the whole temperature range. Apparent emissivity of type 304 stainless steel (SS304) was studied under different oxidizing procedures. Nitrogen and compressed air were input into the system to control the oxidization process. We elucidated the relationship between the apparent emissivity variations and the surface composition changes of SS304 during oxidization. This article aims toward accurate and traceable apparent emissivity data, with well-investigated uncertainty, for use in radiation thermometry.**

***Index Terms*—304 stainless steel, emissivity, oxide, radiation thermometer, uncertainty.**

I. INTRODUCTION

MATERIALS manufactured or processed within high-temperature environments require precise control of temperature to guarantee their quality and to extend their service life [1]–[3]. Compared to traditional temperature measuring methods, such as the use of thermocouples, radiation thermometers provide a noncontact technique that has a fast response time and wide dynamic range and do not contaminate target objects [4], [5]. When the temperature is computed from the radiant power received by a radiometer, emissivity must be understood for each material [6]. Emissivity is defined as the ratio of radiant existence from a material to that emitted from a blackbody at the same temperature, wavelength, and viewing angle. In addition, emissivity is dependent upon surface conditions, including the surface roughness, chemical composition, and microscale structures [7]. Therefore, the development of an instrument for emissivity measurements, with low uncertainty, presents a great challenge in which many variables must be controlled.

Over the several decades since radiation thermometers were first used, various instruments for emissivity measurements have been developed. These can be characterized as either implementing a direct method or an indirect method. In the case of direct methods, emissivity is computed by comparison of the radiance from an opaque sample with that from an approximate blackbody [8], [9]. For indirect methods, emissivity is computed from Kirchhoff's law, after measuring the sample's reflectivity and transmissivity [10]–[12]. Experiments that can measure the temperature dependence of emissivity are typically designed using furnace heating [13]–[15], induction heating, [16] or laser heating [17]–[19]. The first two heating methods offer uniform thermal distributions across the sample. However, these methods have two drawbacks: the highest temperature is limited by the heating power of the system; emissivity is enhanced (i.e., its value is increased) due to radiation from the surroundings. In contrast, the laser heating method can heat samples to particularly high temperatures, though it generates thermal gradients across samples. These aforementioned limitations in emissivity experiments lead to measurements with a high uncertainty and poor repeatability.

Research has also focused on investigating the relationship between the spectral normal emissivity of materials and their surface conditions. Wen and Mudawar [20]–[22] undertook a series of studies in measuring the emissivity of aluminum alloys associated with the surface roughness and assessed results by multispectral radiation thermometry models. Del Campo *et al.* [23] reported the emissivity measurements of oxidized iron below 570 °C. Shi *et al.* [24], [25] investigated the emissivity behavior of oxidized stainless steel between 800 and 1100 K at 1.5 μm. Goett *et al.* [26] measured the emissivity of polished iron above its melting point. Wang *et al.* [27] measured the spectral emissivity of SS304 between 800 °C and 1100 °C with an induction furnace. In spite of a history of publications on the topic of

Manuscript received April 18, 2019; revised July 9, 2019; accepted September 16, 2019. Date of publication September 30, 2019; date of current version June 9, 2020. The work of J. R. Willmott was supported by the Engineering and Physical Sciences Research Council (EPSRC) Fellowship under Grant EP/M009106/1. The Associate Editor coordinating the review process was Mohamed Abou-Khousa. *(Corresponding author: Jon R. Willmott.)*

The authors are with the Electronic and Electrical Engineering Department, University of Sheffield, Sheffield S1 4DE, U.K., and also with the Materials Science and Engineering Department, University of Sheffield, Sheffield S1 4DE, U.K. (e-mail: j.r.willmott@sheffield.ac.uk).

Color versions of one or more of the figures in this article are available online at http://ieeexplore.ieee.org.

Digital Object Identifier 10.1109/TIM.2019.2944504

emissivity, there remain significant gaps in knowledge relating to emissivity measurements.

There are three problems that have not previously been addressed, which cannot be neglected if precise emissivity measurements are to be made. The first problem is the lack of measurement uncertainty information for most emissivity measurements presented in the literature. This, in turn, leads to the second problem of rendering temperature measurement uncertainty calculations, and with it traceability, invalid. For example, the results published by Wen and Mudawar [20]–[22] and Goett *et al.* [26]. Another example is Wang *et al.* [27] who only analyzed instrument uncertainty at one temperature: uncertainty at 1000 °C of 0.0606 (at $k = 2$). Furthermore, the uncertainty introduced by the separation of the sample and the blackbody in their measurements had not been considered. The third problem is the uncertainty introduced by the usual approach of measuring samples within an uncontrolled environmental atmosphere, leading to unrepeatable levels of oxidization. Emissivity of oxidized samples is affected by factors, such as humidity, gas flow speed, heating duration, and heating rate. Unless these problems are resolved, the uncertainty in emissivity measurements can dominate the overall temperature measurement uncertainty [28], e.g., a relatively small emissivity variation of ±0.01 can cause a temperature uncertainty of ±0.70 K at 1000 K, using a 1-μm wavelength thermometer and ±8.00 K using a long-wavelength thermometer, measuring at 10 μm [29]. Thermometer manufacturer data for materials are provided without any assessment of measurement uncertainty, and therefore, it can be seen that uncertainty in the value of a material's emissivity can lead to unacceptable and unknown overall temperature measurement errors. Often, these errors will lead to quality control problems and defects within the manufacturing process [30], [31].

In this article, we evaluate a novel instrument based on the direct emissivity measurement method for measuring apparent normal emissivity of opaque materials under a controlled atmosphere from 973 to 1423 K and a spectral range from 0.85 to 1.1 μm. All measured emissivity references in this article refer to "apparent emissivity," which represents the integral of spectral emissivity over the waveband sensitivity of our radiometers. The uncertainty of our instrument is lower than 0.0590 (at $k = 2$), which was measured and discussed thoroughly over the whole measurement temperature range. The relationship between temperature, emissivity, and oxidizing conditions was studied using the polished samples of type 304 stainless steel. The emissivity measured by our instrument, with fully investigated uncertainty, can be applied in radiation thermometry for input into uncertainty calculations of temperature measurements. Our method is sufficiently adaptable that it could be modified for use at any wavelength relevant to radiation thermometry or thermal imaging by modifying the radiometer and the instrument design parameters. To the best of our knowledge, we have presented the first observations of the connection between the emissivity and the surface composition changes of SS304 during the oxidization process.

II. MEASUREMENT PRINCIPLE

Spectral emissivity quantifies the "efficiency" with which a body radiates thermally, compared to the idealized physical model, known as a blackbody. In radiometry, spectral emissivity, $\varepsilon(\lambda, T)$, is the ratio of radiant power emitting from a body to that from a blackbody at the same temperature

$$\varepsilon(\lambda, T) = \frac{L(\lambda, T)}{L_b(\lambda, T)} \tag{1}$$

where λ is the wavelength, T is the temperature, $L(\lambda, T)$ is the radiance from a body, and $L_b(\lambda, T)$ is the radiance from a blackbody.

The spectral radiance of a blackbody, $L_b(\lambda, T)$, can be expressed by Planck's law

$$L_b(\lambda, T) = \frac{C_1}{\lambda^5(e^{C_2/\lambda T} - 1)} \tag{2}$$

where $C_1 = 1.191 \times 10^8\ \mathrm{W} \cdot \mu\mathrm{m}^4 \cdot \mathrm{m}^{-2} \cdot \mathrm{Sr}^{-1}$ is the first radiation constant and $C_2 = 1.439 \times 10^4\ \mu\mathrm{m} \cdot \mathrm{K}$ is the second radiation constant [7].

In our emissivity measurements, optical detectors simultaneously receive radiant power emitting from a sample and a blackbody, P_s and P_b, and convert them into electrical signals

$$P_s(\lambda, T_s) = \Omega_s A_s \tau_o \int_{\lambda_1}^{\lambda_2} \varepsilon_s(\lambda, T_s) L_b(\lambda, T_s) s_s(\lambda) \tau_s(\lambda) d\lambda \tag{3}$$

$$P_b(\lambda, T_b) = \Omega_b A_b \tau_o \int_{\lambda_1}^{\lambda_2} L_b(\lambda, T_b) s_b(\lambda) \tau_b(\lambda) d\lambda \tag{4}$$

where the subscript "b" denotes blackbody, the subscript "s" denotes sample, Ω is the solid angle, A is the measurement area upon the target, τ_0 is the propagation coefficient of the atmosphere, $s(\lambda)$ is the relative spectral responsivity of detectors, and $\tau(\lambda)$ is the total transmissivity of the optical path.

The spectral responsivity of a detector and total transmissivity of a radiometer's optical path are the functions of wavelength. If a narrow bandpass filter is used in the system, these two factors can be regarded as independent of wavelength [32]. The solid angle, measurement area, and spectral responsivity difference between two identical radiometers can be reduced to an acceptable level if they are calibrated and corrected carefully, which implies that $\Omega_s \approx \Omega_b$, $A_s \approx A_b$, and $s_s(\lambda) \approx s_b(\lambda)$. When radiometers are placed within a stable environment, the transmissivity of the optical paths of the sample and the blackbody are similar, leading to the elimination of $\tau_s(\lambda)$ and $\tau_b(\lambda)$. The spectral emissivity of a sample then can be expressed as

$$\varepsilon_s(\lambda, T) \approx \frac{P_s(\lambda, T_s)}{P_b(\lambda, T_b)}. \tag{5}$$

In actual working conditions, a radiometer receives power not only from a sample but also from its surroundings: by background radiation, reflection, and scattering. This leads to an apparent, unwanted, increase in emissivity. The total radiant

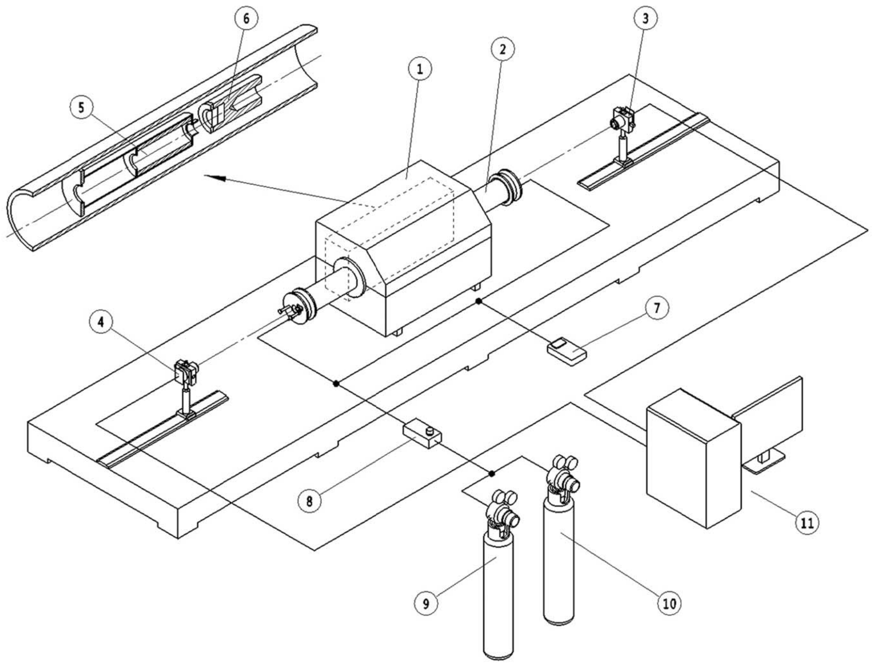

Fig. 1. Schematic of the emissivity measurement instrument construction. Split furnace, Carbolite HST 12/400 (1), ceramic tube (2), radiometer I at the blackbody side (3), radiometer II at the sample side (4), radiation shield (5), sample-blackbody component (6), oxygen meter (7), flowmeter (8), nitrogen cylinder (9), compressed air cylinder (10), and data acquisition system (11).

power measured by a radiometer can be expressed as

$$P_{s,\mathrm{meas}}(\lambda,T)=P_s(\lambda,T)+P_{\mathrm{sur},rfl}(\lambda,T)+P_{\mathrm{sur}}(\lambda,T)+P_{s,rfl}(\lambda,T)+P_{\mathrm{mult}-rfl}(\lambda,T) \quad (6)$$

where $P_s(\lambda,T)$ is the measured radiant power from a sample, $P_{\mathrm{sur},rfl}(\lambda,T)$ is the measured radiant power from surroundings reflected by a sample, $P_{\mathrm{sur}}(\lambda,T)$ is the measured radiant power from surroundings, $P_{s,rfl}(\lambda,T)$ is the measured radiant power from a sample reflected by surroundings, and $P_{\mathrm{mult}-rfl}(\lambda,T)$ is the measured radiant power from a sample or surroundings reflected multiple times.

For an opaque object, reflectivity and emissivity can be described by Kirchhoff's law. In this article, the reflectivity can be treated as bidirectional or directional hemispherical quantity depending on the object's surface type

$$\varepsilon=1-\rho \quad (7)$$

where ρ is reflectivity.

If the measurement area is strictly limited within the sample surface, radiation from outside the measurement area can only be received following scattering. In (6), $P_{\mathrm{sur}}(\lambda,T)$, $P_{s,rfl}(\lambda,T)$, and $P_{\mathrm{mult}-rfl}(\lambda,T)$ are small quantities compared to the first two terms, which can be omitted. Therefore, the measured radiant power of a radiometer can be simplified to

$$\begin{aligned}P_{s,\mathrm{meas}}(\lambda,T)&=\Omega_s A_s \tau_o\int_{\lambda_1}^{\lambda_2}\varepsilon_s(\lambda,T_s)L_b(\lambda,T_s)s_s(\lambda)\tau_s(\lambda)d\lambda\\&\quad+(1-\varepsilon_s(\lambda,T_s))\Omega_s A_s\tau_o\int_{\lambda_1}^{\lambda_2}\varepsilon_{\mathrm{sur}}(\lambda,T_{\mathrm{sur}})\\&\quad\times L_b(\lambda,T_{\mathrm{sur}})s_s(\lambda)\tau_s(\lambda)d\lambda \quad (8)\end{aligned}$$

where T_s is the temperature of sample, $\varepsilon_{\mathrm{sur}}(\lambda,T_{\mathrm{sur}})$ is the emissivity of surroundings, and T_{sur} is the temperature of the surroundings.

In this article, we used a cold, high emissivity, radiation shield to block the background radiation from the furnace tube during measurements, which represents $\varepsilon_{\mathrm{sur}}\approx 1$ and $T_{\mathrm{sur}}\ll T_s$. Therefore, the emissivity measured can be expressed as

$$\varepsilon_s(\lambda,T)\approx\frac{P_{s,\mathrm{meas}}(\lambda,T_s)}{P_b(\lambda,T_b)}. \quad (9)$$

III. INSTRUMENT DESIGN AND EXPERIMENTAL METHODS

A. Emissivity Measurement Instrument

The emissivity measurement instrument was composed of a split furnace, two radiometers, a radiation shield, a sample-blackbody component, and the gas system. The schematic of the instrument construction is shown in Fig. 1. The radiation shield and sample-blackbody component were placed inside the furnace ceramic tube, as shown in Fig. 2.

A commercial split tube furnace was positioned upon an optical table. The sample-blackbody housing was placed in the middle of the furnace tube. A sample was mounted within the sample recess, opposite to the blackbody cavity, and fixed tightly by a sample locking ring. Two type K thermocouples were embedded within the sample assembly to monitor the temperature of the cavity and the sample but not to take part in the emissivity measurement itself. One of these was inserted into a hole adjacent to the cavity and the other was embedded adjacent to the sample. The sample, blackbody, and thermocouple were designed to achieve good thermal equilibrium by means of machining the assembly from a single piece of Inconel.

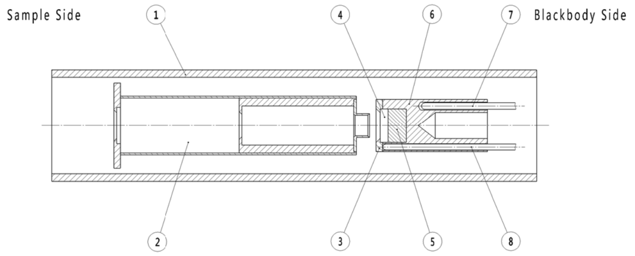

Fig. 2. Cross-sectional diagram of the furnace ceramic tube (top view). Ceramic tube (1), radiation shield (2), sample locking ring (3), sample (4), adjusting block (5), sample-blackbody housing (6), cavity thermocouple, TC Direct 405-038-Class 1 (7), and sample thermocouple, TC Direct 405-038-Class 1 (8).

TABLE I
PARAMETERS OF THE RADIOMETERS

Wavelength	0.85 to 1.1 μm
Focal length	60 mm
F-number	3.0
Object distance	1.00 m
Field of View	80:1

Inside the tube, a movable radiation shield was placed over the sample for a very brief period during the measurement to prevent background radiation from reaching the radiometer. Outside the tube, an optical switch was fixed on the tube end at the sample side to indicate the start of valid data recorded when the radiation shield achieved its correct position for the measurement. Two custom fabricated radiometers were placed at the blackbody side and the sample side, identified as radiometers I and II, respectively. They were aligned and fixed upon the optical table before each measurement.

A methodology was devised and used to control the atmosphere surrounding the sample, within the furnace tube. Compressed air and nitrogen were input into the sealed tube in ratios determined by a valve mechanism. Compressed air was input to grow oxide layers upon the sample in a controlled fashion, while nitrogen was added to protect the sample from oxidizing. The gas flow rate was adjusted and monitored by a flowmeter with a scale that ranged from 0.1 to 0.5 L/min (lpm). The oxygen level inside the tube was monitored by an oxygen meter that was connected to the gas line.

1) *Radiometers:* Two radiometers were custom fabricated and calibrated to achieve measurements that were identical: within our ability to measure the differences between them. The radiometer was designed as a common-path optical system with a red laser (650 nm) and a silicon (Si) photodiode. The red laser was used as a sight alignment tool for measurements. The parameters of the radiometer are listed in Table I. The schematic of a radiometer is shown in Fig. 3. The lens selected for the radiometer was a commercial 60-mm focal length singlet. The detector module consisted of an RG850 filter, a 0.2-mm-diameter field aperture, and a Si photodiode. The spectral responsivity of the radiometer is shown in Fig. 4.

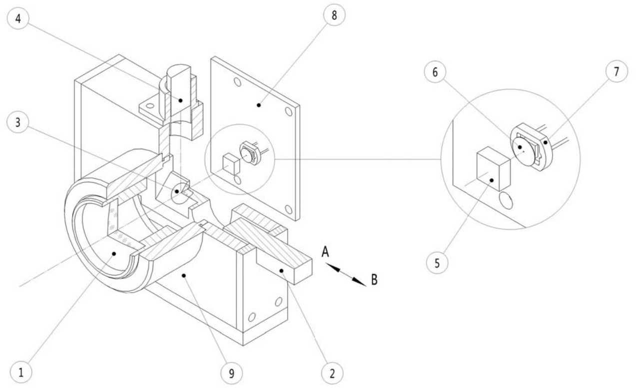

Fig. 3. Schematic of our radiometer. Singlet lens, Edmund optics #45-127 (1), slide block (2), flat mirror (3), laser module (4), RG850 filter, Edmund optics 66-107 (5), 0.2 mm diameter field aperture (6), Si photodiode, Hamamatsu S1133-01 (7), PCB (8), and radiometer brackets (9). The slide block, which was designed with a mirror and a hole, was used to switch the optical paths between the red laser and Si photodiode, either at position A or B.

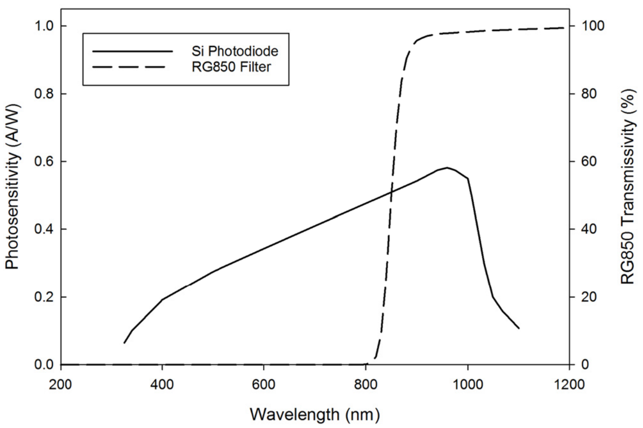

Fig. 4. Spectral responsivity of our radiometers. The right axis represents the photosensitivity of the Si photodiode. The left axis represents the transmissivity of the 3-mm-thick RG850 filter.

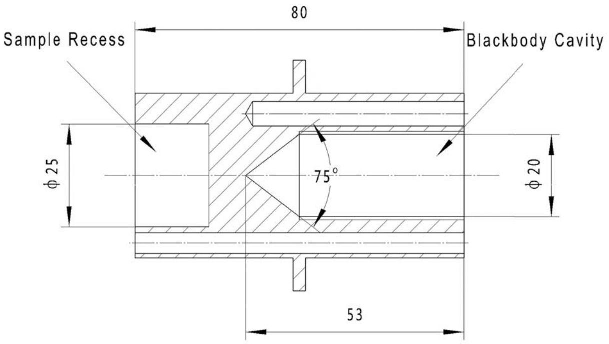

Fig. 5. Cross-sectional diagram of the sample-blackbody housing. The dimension of the sample recess was 25 mm in diameter × 6 mm thick. The dimension of the blackbody cavity was 20 mm in diameter × 53 mm long. The bottom of the blackbody cavity was machined with a 75° cone.

2) *Sample-Blackbody Housing:* The cross-sectional diagram of the sample-blackbody housing is shown in Fig. 5. A sample recess and a cavity were machined on each side of the housing. The cavity wall was

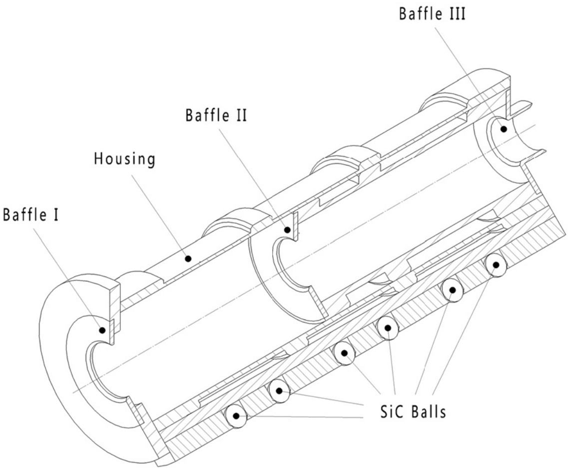

Fig. 6. Cross-sectional diagram of the radiation shield.

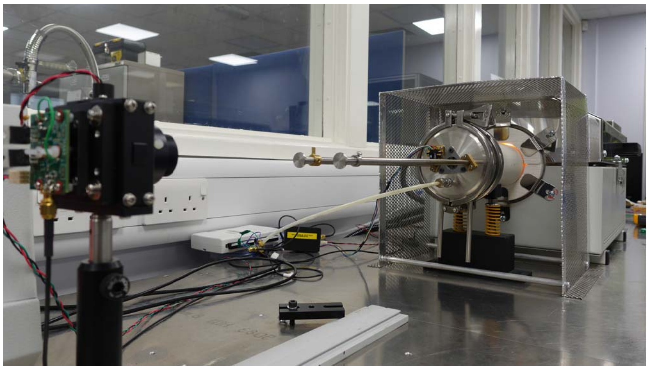

Fig. 7. Photograph of our emissivity instrument when measuring emissivity at a sample temperature of 1423 K. The photograph is taken from the sample side; the radiation shield pusher rod can be seen projecting from the furnace. One of the two radiometers can be seen to the left of the figure.

turned with threads and painted with high emissivity material, HiE-Coat 840-MX, to increase the effective emissivity, which was above 0.996 according to Gouffe's theory [33]. Our sample-blackbody housing was designed for three specific benefits. First, both the sample and the blackbody cavity were heated in the thermal equilibrium area of a furnace and, therefore, their temperatures can be considered to be identical. Second, the blackbody cavity was designed to have a stable radiance temperature with defined effective emissivity. Finally, the blackbody cavity was designed to match the measurement area of our radiometers, leading to a low uncertainty even in the presence of the size of source effect (SSE) [34].

3) *Radiation Shield:* A radiation shield was used to eliminate the illumination received by the sample from the hot tube wall. The cross-sectional diagram of the radiation shield is shown in Fig. 6. The shield was composed of a stainless steel housing and three optical baffles placed along the housing. In addition, the internal shield surface was coated with HiE-Coat 840-MX to absorb stray radiation. Two rows of SiC balls were mounted in the bottom of the shield, which enabled it to be moved from the tube end to the center within 2 s: minimizing disruption to furnace thermal equilibrium.

B. Measurement Procedure

The first step in our emissivity measurements was to mount the sample inside the sample-blackbody housing. The housing was then pushed to the center of the furnace tube. The two radiometers were aligned and focused on the conical section of the blackbody cavity and the sample center, respectively. With the furnace stabilized at the set target temperature, the data acquisition system started to log the measured output from the radiometers, while recording the measured sample radiation, the radiation shield was pushed into the tube to cover the sample. As soon as the shield was in position, the optical switch was triggered to indicate the start of valid data. Following completion of data acquisition, the shield was then retracted and the furnace was set to the next temperature point, allowed to stabilize in temperature and a new measurement was taken. Fig. 7 shows a photograph of our instrument during emissivity measurements at a sample temperature of 1423 K.

C. Sample Preparation

Commercial grade type 304 stainless steel samples were prepared for the emissivity measurement. The emissivity of this material has been studied by several researchers using various temperature conditions and wavelengths previously [20], [24]. Although the emissivity of SS304 between 0.85 and 1.1 μm has not been published, the data from the previous studies can be considered as the reference results to evaluate the performance of our emissivity measurement instrument.

Samples were cut to 25 mm in diameter by 6 mm thick from an SS304 rod. The top flat surface was ground by P240, P400, and P800 grinding papers and polished to 3 μm by diamond suspensions. Samples were ultrasonically cleaned using isopropyl alcohol, fully dried, and stored in a vacuum box prior to the measurements.

D. Measurement Strategy

Samples were divided into two sets for different measurement methods. The first set was free from deliberate oxidization to enable a comparison with previous work. This set of samples was measured within a nitrogen atmosphere at five temperatures: 973, 1073, 1173, 1273, and 1423 K. The second set was oxidized, with the aim of measuring apparent emissivity trends under different oxidizing conditions. This set was processed as follows. At first, a sample was heated within a nitrogen atmosphere to 973 K. After the furnace had stabilized for 30 min, air was input into the furnace tube at a flow rate of 0.5 lpm, to displace the nitrogen, for oxidizing the sample. Emissivity was measured every 10 min during the whole oxidizing period. Other samples were measured with the same oxidizing procedure at 1073, 1173, 1273, and 1423 K.

IV. INSTRUMENT MEASUREMENT UNCERTAINTY

The uncertainties in our measurement can be categorized into three main sources: the approximate nature of the cavity blackbody, the characteristics of the radiometers, and the operational procedures. The radiant power measured by the radiometers was affected by the size of the source effect [34], responsivity correction, and electronic noise. Furthermore, operational procedures also introduced uncertainties, such as the misalignment and the perturbation that was due to the radiation shield. In this article, uncertainties were assumed to be uncorrelated with each other [35]. Equation (5) can be rewritten to (10) for analyzing uncertainties quantitatively

$$\varepsilon_s = \frac{P_s(T_s)}{P_b(T_b)} \cdot \frac{\Omega_b A_b s_b \tau_b L_b(T_b)}{\Omega_s A_s s_s \tau_s L_s(T_s)} \tag{10}$$

where $L_s(T_s)$ and $L_b(T_b)$ are the radiance of a sample and an ideal blackbody in the spectral range between 0.85 and 1.1 μm.

The square of the combined standard uncertainty $u_c(x)$ is expressed by [36]

$$[u_c(x)]^2 = \sum_{i=1}^{N} [u(x_i)]^2 \tag{11}$$

where $u(x_i)$ is a standard uncertainty component.

A. Blackbody Emissivity—Isothermal

The custom-designed cavity blackbody applied in this article is not an ideal blackbody, whose effective emissivity can be determined by the wall emissivity, geometry factors, and machining imperfections under isothermal conditions [37], [38]. The geometry of our blackbody cavity may have deviated from the design due to manufacturing errors, leading to the imperfections in the cavity shape. Assuming that the cavity was machined to the required mechanical tolerances, the geometry was maintained to ±0.2 mm in length and ±0.5° in angle. The maximum uncertainty (at $k = 2$) was estimated to 0.0142 over the whole temperature range.

B. Blackbody Emissivity—Nonisothermal

The effective emissivity of a cavity blackbody decreases under nonisothermal conditions due to nonuniform thermal distributions along the cavity. This distribution is affected by two factors: the thermally uniform length of the furnace and the heat exchanged between the cavity and its surroundings. The maximum uncertainty (at $k = 2$) was estimated to 0.0080.

C. Blackbody Cavity Radiance Temperature

To assess the radiance temperature of our approximate blackbody cavity, a class-1 thermocouple was inserted alongside the cavity and in thermal contact with it. The uncertainty in the radiance temperature of the blackbody was, therefore, equivalent to the uncertainty of the thermocouple.

D. Size of Source Effect

The SSE of each radiometer was measured to calculate the area over which the measurement area impinged upon the blackbody cavity and the sample. SSE describes the phenomenon that a radiometer receives radiation from the region outside the nominal measurement area. It arises as a consequence of optical aberrations, diffractions, reflections, and scattering between lens interfaces [34]. SSE can be characterized using direct [39], indirect [40], and scanning methods [41]. In this article, the direct method was applied, which is expressed (12). The background radiation was assumed to be neglected for measurements above 200 °C [42]

$$\sigma_S(r, r_{\max}) = \frac{S(r, L)}{S(r_{\max}, L)} \tag{12}$$

where r is the radius of the aperture, $r_{\max}$ is the size of the maximum aperture, L is the working distance, $S(r, L)$ is the signal at the radius r, and $S(r_{\max}, L)$ is the signal at the maximum aperture.

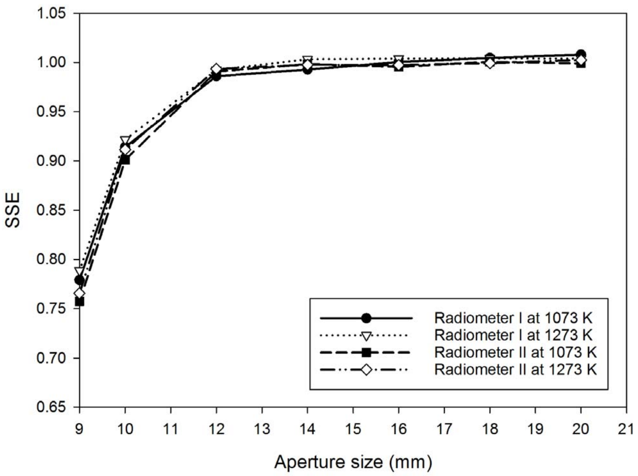

Fig. 8. SSE of our radiometers measured at 1073 and 1273 K. The ordinate axis is normalized against the measurement area, which was 9 mm in diameter at a distance of 1 m. When the aperture was greater than 14 mm in diameter, SSE of each radiometer was close to 1. The slight fluctuations were caused by the electronic noise of the radiometers or the temperature drift of the furnace.

The SSE for our radiometers measured at 1073 and 1273 K is shown in Fig. 8. The nominal design measurement of 14 mm in diameter was used as the reference measurement area, which was smaller than 25-mm-diameter samples.

E. Responsivity Correction

Emissivity was computed by taking the ratio of the signals from two identical (by design) radiometers. There were slight differences in responsivity of these radiometers due to the variation in spectral response of photodiodes and the transmissivity of optical elements. In this article, both radiometers were corrected against a calibrated blackbody furnace, Landcal R1500 T. The responsivity of radiometer II was corrected to match that of radiometer I by applying least square fitting [43]. The correction is shown in Fig. 9, with the maximum uncertainty (at $k = 2$) calculated to be 0.0029.

F. Temperature Fluctuation of the Sample and the Radiation Shield

A measurement time of 1 s was required to record the valid data. With the radiation shield in place during this period, the temperature of the sample decreased, while the temperature of the shield increased. A numerical model was built in Ansys Icepak to analyze their thermal conditions dynamically.

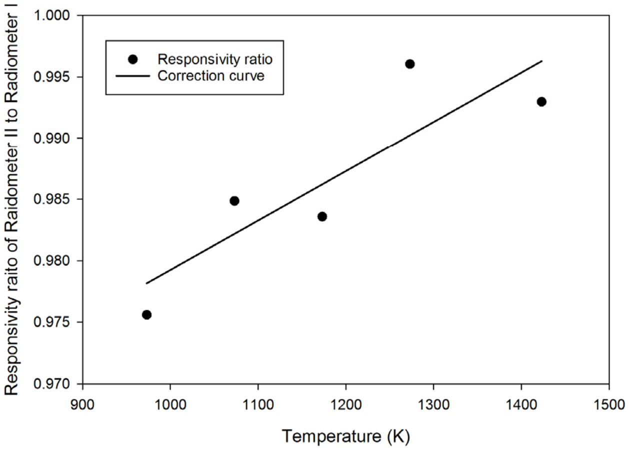

Fig. 9. Spectral responsivity correction of the radiometers.

TABLE II

RADIANCE INCREASE OF THE RADIATION SHIELD

Time (s)	Relative radiance increase (0.85 to 1.1 μm)				
	430.5 K	454.0 K	485.5 K	517.0 K	580.0 K
0.00	0.0000	0.0000	0.0000	0.0000	0.000
1.00	5.67E-09	9.58E-09	2.47E-08	5.72E-08	3.97E-07
2.00	1.25E-08	2.24E-08	5.90E-08	1.39E-07	1.01E-06
3.00	3.34E-08	6.30E-08	1.95E-07	5.10E-07	4.09E-06

TABLE III

RADIANCE DECREASE OF A SAMPLE

Time (s)	Relative radiance decrease (0.85 to 1.1 μm)				
	973.0 K	1073.0 K	1173.0 K	1273.0 K	1423.0 K
0.00	0.0000	0.0000	0.0000	0.0000	0.0000
1.00	-0.6878	-0.9520	-1.3955	-1.8390	-2.8000
2.00	-1.4122	-1.9420	-2.8233	-3.7047	-5.6133
3.00	-2.1973	-2.9983	-4.3153	-5.6323	-8.3833

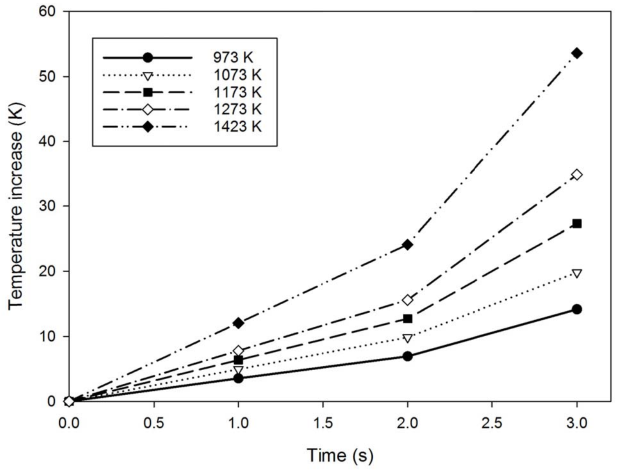

Fig. 10. Temperature increase of the radiation shield.

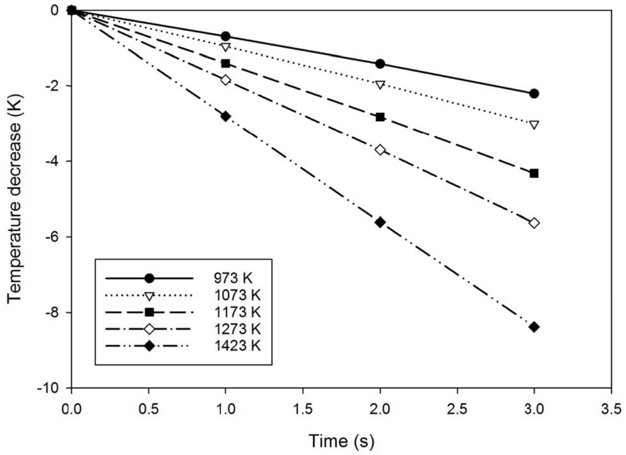

Fig. 11. Temperature decrease of the sample.

The radiance changes are listed in Tables II and III. The temperature change of the radiation shield and the sample are shown in Figs. 10 and 11, respectively. The thermally induced radiance increase in the radiation shield was close to zero in our experiments; according to Planck's law, the wavelength of the increased radiance was outside the responsivity spectrum of the radiometers [44].

The temperature of samples was monitored by a thermocouple during emissivity measurements. When developing our instrument, we found that if the time it took to move the radiation shield into place was no more than 2 s, the measured temperature decrease was lower than the simulation result. We, therefore, used the simulation result in the calculation of maximum uncertainty.

G. Temperature Difference Between the Sample and the Cavity Blackbody

The sample and the blackbody were placed in approximate thermal equilibrium by design. The actual temperature difference was measured using two thermocouples over the range of 973–1423 K. The recorded difference ranged within ±1 K, which equated to the uncertainties (at $k = 2$) from 0.0014 to 0.0051.

H. Electronic Noise

The radiometer output fluctuated during the course of the measurement, adding additional uncertainty due to electronic noise within the radiometers. This uncertainty increased at the lower end of the temperature range, due to the lower signal-to-noise ratio, as a result of the reduced power from the target. The uncertainties (at $k = 2$) due to radiometer noise ranged from 0.0141 to 0.0002 and 0.0160 to 0.0003 between 973 and 1423 K for radiometers I and II, respectively.

I. Positioning

Measurement uncertainty was introduced during sample loading due to the working distance variations between the measurements. Other components were permanently located on the optical table and, therefore, did not contribute to this uncertainty. The positional uncertainty of the housing was estimated to be ±1 mm, with a maximum uncertainty (at $k = 2$) estimated to be 0.0080.

TABLE IV

COMBINED STANDARD UNCERTAINTIES (UNITLESS) OF THE INSTRUMENT

	Uncertainty	Quantity	At 973 K (k=2)	At 1073 K (k=2)	At 1173 K (k=2)	At 1273 K (k=2)	At 1423 K (k=2)
Blackbody	Blackbody emissivity, Isothermal	$u_1(L_{b,i})$			0.0142		
	Blackbody emissivity, Non-isothermal	$u_2(L_{b,i})$			0.0080		
	Blackbody radiance temperature	$u_3(L_{b,i})$	0.0481	0.0455	0.0430	0.0408	0.0378
Radiometer	Size of source effect for radiometer I	$u_4(SSE_i)$	0.0014*	0.0013	0.0030*	0.0012	0.0011*
	Size of source effect for radiometer II	$u_5(SSE_i)$	0.0029*	0.0023	0.0013*	0.0011	0.0003*
	System responsivity correction	$u_6(S_i)$			0.0029		
	Noise for radiometer I	$u_7(S_i)$	0.0141	0.0052	0.0016	0.0008	0.0002
	Noise for radiometer II	$u_8(S_i)$	0.0160	0.0041	0.0016	0.0009	0.0003
Radiation shield	Temperature decrease of the sample	$u_9(L_{s,i})$	0.0186	0.0210	0.0253	0.0281	0.0336
	Temperature increase of the radiation shield	$u_{10}(L_{s,i})$	-	-	-	-	-
In-use	Temperature difference between a sample and a blackbody	$u_{11}(L_{b,i})$	0.0034	0.0014	0.0036	0.0051	0.0041
	Positioning	$u_{12}(S_i)$			0.0080		
	Combined standard uncertainty	$u_c(\varepsilon_s)$	0.0590	0.0538	0.0535	0.0531	0.0540

Note: "*" indicates interpolated data.

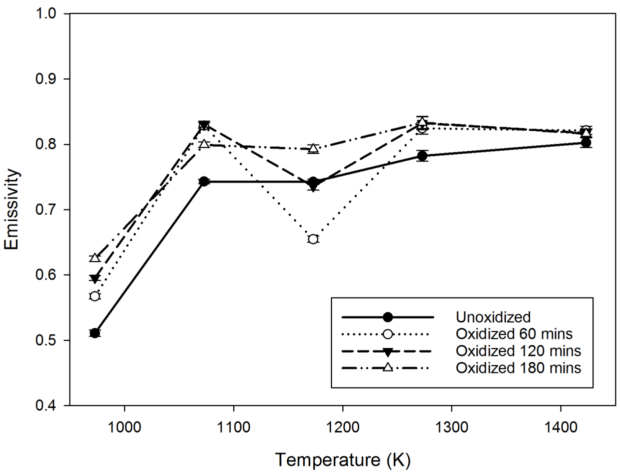

Fig. 12. Data for apparent emissivity as a function of temperature of SS304.

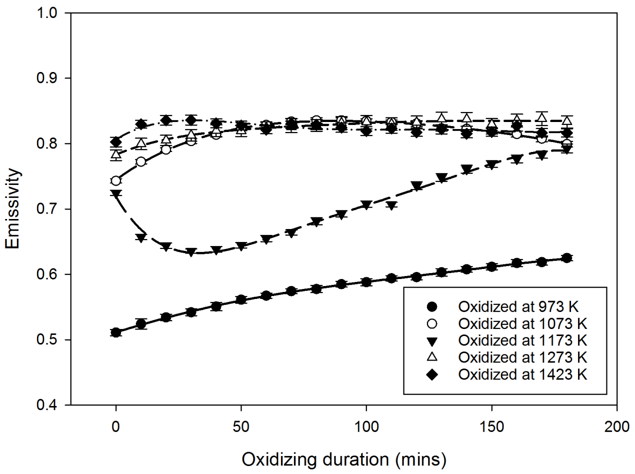

Fig. 13. Apparent emissivity as a function of oxidizing duration for SS304.

J. Combined Standard Uncertainties of the Instrument

For all factors discussed earlier, the uncertainty of measurements can be calculated by (11). From 973 to 1423 K, the maximum combined standard uncertainty was 0.0590 (at $k = 2$), as shown in Table IV.

V. RESULTS AND DISCUSSION

A. Apparent Emissivity of SS304

Fig. 12 shows the apparent emissivity data for SS304 samples from 973 to 1423 K. The lines represent the emissivity of samples without deliberate oxidization and samples oxidized for 60, 120, and 180 min. Emissivity of all our samples was measured to lie between 0.5108 and 0.6248 at 937 K and then converged to around 0.8 at 1423 K. The curves show a similar trend for each sample: emissivity increased from 937 to 1073 K, reduced from 1073 to 1173 K, and increased again from 1173 to 1423 K.

Fig. 13 shows the apparent emissivity data for samples oxidized by different procedures. The symbols represent emissivity measured at 10-min intervals. Curves were fit by the fifth-order polynomial equations for each set of data. For the sample oxidized at 973 K, emissivity increased from 0.5108 to 0.6248 continuously. At 1073 K, emissivity increased in the first 80 min and then decreased to 0.7992 after 180 min. At 1173 K, emissivity decreased to 0.6356 in the first 30 min and then increased to 0.7926. At 1273 K, emissivity increased rapidly to 0.8197 in the first 40 min and stabilized at around 0.8000. At 1423 K, emissivity increased to 0.8356 in the first 20 min and then fluctuated in the region of 0.8000. Each curve shows a unique trend, which suggests a complex emissivity behavior under different oxidizing procedures.

TABLE V

APPARENT NORMAL EMISSIVITY OF SS304

Oxidization duration (minutes)		0	10	20	30	40	50	60	70	80	90
Oxidization temperature	973 K	0.5108	0.5241	0.5341	0.5419	0.5507	0.5612	0.5673	0.5742	0.5774	0.5849
	1073 K	0.7431	0.7723	0.7908	0.8039	0.8135	0.8237	0.8286	0.8336	0.8354	0.8354
	1173 K	0.7246	0.6570	0.6438	0.6356	0.6383	0.6445	0.6547	0.6642	0.6815	0.6926
	1273 K	0.7822	0.7996	0.8050	0.8127	0.8197	0.8196	0.8245	0.8257	0.8277	0.8316
	1423 K	0.8025	0.8298	0.8356	0.8361	0.8311	0.8277	0.8213	0.8308	0.8289	0.8245
Oxidization duration (minutes)		**100**	**110**	**120**	**130**	**140**	**150**	**160**	**170**	**180**	
Oxidization temperature	973 K	0.5879	0.5938	0.5954	0.6030	0.6076	0.6115	0.6172	0.6185	0.6248	
	1073 K	0.8346	0.8326	0.8307	0.8233	0.8227	0.8188	0.8147	0.8075	0.7992	
	1173 K	0.7076	0.7069	0.7358	0.7483	0.7610	0.7689	0.7766	0.7832	0.7926	
	1273 K	0.8329	0.8301	0.8324	0.8374	0.8373	0.8294	0.8353	0.8381	0.8333	
	1423 K	0.8192	0.8234	0.8174	0.8220	0.8152	0.8178	0.8274	0.8167	0.8164	

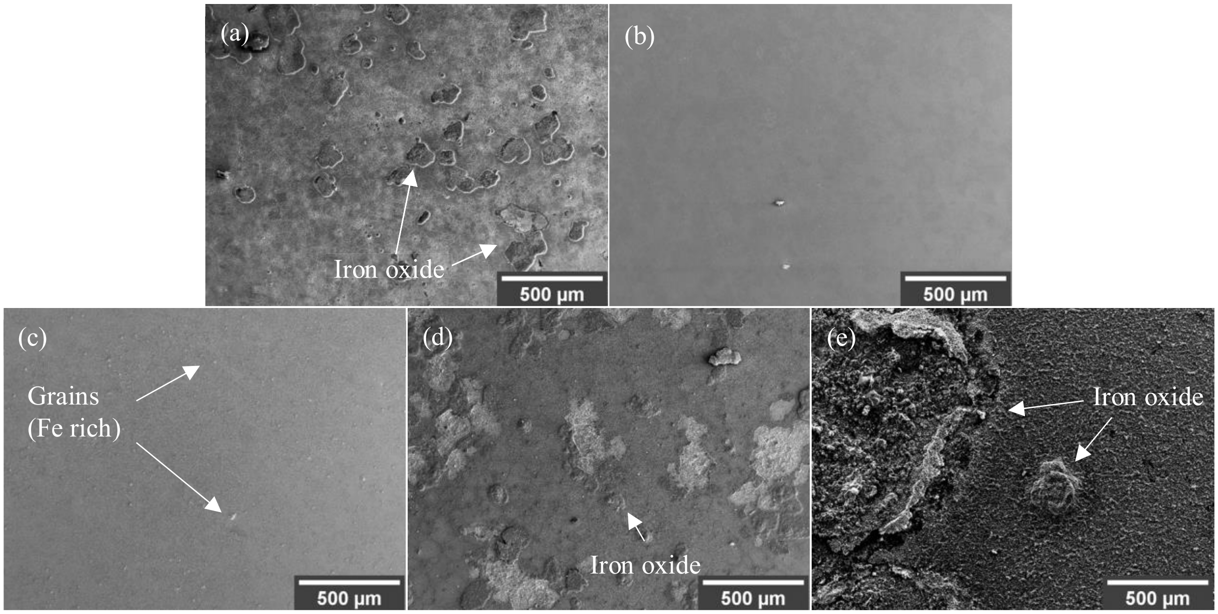

Fig. 14. Surface SEM images of samples oxidized by different strategies. (a) 973 K. (b) 1073 K. (c) 1173 K. (d) 1273 K. (e) 1423 K.

Table V shows the apparent normal emissivity of SS304 under each oxidization procedure.

At each measured temperature, the variation in emissivity may represent the variation of surface conditions. We find that the surface of a sample oxidized at 1173 K changed dramatically during the measurement. On the other hand, the surface of a sample oxidized a 1423 K was more stable than the samples oxidized at other temperatures.

TABLE VI

EDX RESULTS OF SAMPLES

Sample oxidization temperature (K)	Atomic weight (%) O	Cr	Fe	Mn
973	45.7	23.1	10.1	7.2
1073	25.3	16.0	39.1	3.0
1173	42.8	21.2	16.7	6.1
1273	49.7	25.4	14.8	7.3
1423	48.3	18.6	13.4	11.9

B. SEM and Energy-Dispersive X-Ray Analysis Results of SS304

Fig. 14 shows the surface SEM images of SS304 samples used in our emissivity measurements. These samples were observed after oxidizing for 180 min by different procedures. SEM images were taken from areas within the emissivity measurement area. As shown in Fig. 14(a), iron oxide islands [as determined by energy-dispersive x-ray analysis (EDX), with area average compositions summarized in Table VI] can be observed to grow on top of a Cr and CrMn (white areas) oxide layer. In Fig. 14(b), the top oxide layer is continuous and is dominated by Fe oxide that contains a small number of particulates. In Fig. 14(c), Fe-rich particles are randomly distributed on an otherwise continuous appearing Cr oxide layer with a number of small particles (pointed out by arrows). In Fig. 14(d), iron oxide islands occupy much of the surface in nickel-enriched or manganese-enriched forms. In Fig. 14(e), iron oxide islands grow much bigger, some of them are larger than the SEM image shows, and occupy most of the surface. Separations of some islands can be observed on the top surface.

C. Discussion

The apparent emissivity of SS304 measured in this article can be compared with the previous measurements published by Shi *et al*. [24] and Liu *et al.* [45]. At 973 K, the emissivity of our samples without deliberate oxidization was around 0.51, which is lower than the result of 0.60 measured by Shi *et al*. [24]. At 1073 K, emissivity without oxidization, measured by our instrument, was around 0.74, which is equivalent to the result of Shi *et al*. [24]. At 973 K, the emissivity of samples oxidized for 180 min, measured in this article, was around 0.62, which was slightly lower than the results obtained by Shi *et al*. [24] and Liu *et al.* [45]. At 1073 K, the emissivity of our samples oxidized for 180 min was around 0.8, which is equivalent to the result of Shi, but slightly higher than the result of Liu. Considering that the results published by Shi and Liu were measured at 1.5 μm and their samples had a different surface finish and experienced different oxide growth conditions, we consider the measurements obtained by our instrument to be in agreement with these previously published results.

The apparent emissivity of SS304, as shown in Figs. 12 and 13, was proportional to the oxidizing duration at 973 K only. SEM images indicate that the increased size of iron oxide islands with increased oxidation time may cause the steady emissivity increase. In contrast to 1273 K, for both unoxidized and oxidized samples, their emissivities were measured to be around 0.8 above 1273 K, reaching a stable value after approximately 50 min, which indicates that their surface conditions became stable quickly at this temperature range. However, the emissivity behavior was much more complex at 1073 and 1173 K. At 1073 K, emissivity reached the highest value after 90 min and then reduced to around 0.8 after 180 min. At 1173 K, emissivity decreased quickly in the first 30 min and then increased to 0.78 by the end of the measurement. Notably, the final emissivity values (after oxidation for 180 min) for oxidation at both 1073 and 1173 K are identical, while the chemical composition (see Table VI) is not. What is very similar, however, for both these surfaces is the presence of continuous and fairly smooth oxide layers. Hence, we conclude that the surface condition of the samples changed dramatically under different oxidizing procedures and the observed emissivity changes are likely to reflect the changes in oxidation stages/mechanisms, e.g., effects such as island versus continuous coverage, which can be reliably detected with our instrument.

Previous research indicates that the emissivity variation of steel can be associated with the surface oxide condition dynamically [46]. From our results, we find that the emissivity of oxidized samples also strongly depends upon oxide processes, including the oxide temperature, duration, and rate. The aforementioned analysis, using SEM images and EDX spectra, shows that SS304 oxidizes slowly when heated in dry air below 1173 K, which has an oxide composition of Cr_2O_3 and iron oxide (FeO or Fe_3O_4) [47]. From 1173 to 1273K, the oxide layer grows at a parabolic rate, with two stages. At the first stage, Cr_2O_3 forms and covers the substrate tightly. At the second stage, iron starts to penetrate into the Cr_2O_3 layer from grain boundaries and forms iron oxide particles at a higher oxidization rate [48]. Above 1273 K, the iron oxide grows quickly and occupies the majority of the top surface, after 20 min [49]. At the same time, the enrichment of manganese continuously occurs at high temperatures [50].

The emissivity measurements of SS304 samples in this article, oxidized with each of the aforementioned processes, are in accordance with the oxide behavior from 973 to 1423 K, shown in the literature. At 973 K, the increase in emissivity may imply the growth of a Cr_2O_3 layer and the emergence of iron islands. At 1073 K, the decrease in emissivity may imply that iron started to penetrate into the surface after the Cr_2O_3 layer reached its maximum thickness. At 1173 K, the rapid decrease in emissivity may imply that iron penetrated quickly and then formed iron oxides, leading to increased emissivity. At 1273 K, iron oxides grew fast and then became stable under this condition. At 1423 K, iron oxides grew much bigger and started to separate from the substrate.

In this article, the initial surface condition of the samples could also have had an effect upon the measurements, including the surface roughness and surface damage that may have been introduced during the polishing process. Our samples were polished to 3 μm by diamond suspension, though the fluctuation of the surface was greater than the measurement wavelengths of 0.85–1.1 μm. In this roughness range, emissivity is highly sensitive to the surface geometry, especially on the surface slope at the microscale [22]. Meanwhile, the preparation method can also damage the surface grain boundary of the material and change the grain size. Surface damage, such as this, can accelerate the iron oxidization rate at higher temperatures, leading to the emissivity change [51]. These two factors may introduce new uncertainties for the emissivity measurements of SS304 and should be investigated in more detail in the future.

VI. CONCLUSION

Accurate knowledge of the emissivity of materials is essential if accurate noncontact temperature measurements are to be made. We presented a novel instrument for the measurement of apparent normal emissivity of target samples over a temperature range of 973–1423 K under a controlled atmospheric environment. Instrumental uncertainty was measured and analyzed thoroughly, and this was in pursuit of our aim of enabling traceability of emissivity measurements to the SI. Our measurements are particularly applicable to metal and petrochemical industries, which require precise emissivity measurements. For example, petrochemical furnaces and steel ladles alike require a balance between high temperatures for efficient production and low temperatures for longevity of assets. Precise emissivity measurements promise to obviate the current uncertainty in using radiation thermometry for these measurements. The apparent emissivity of type 304 stainless steel was measured in the oxidized conditions and with samples polished to 3 μm finish. For oxidized samples, their surface topography was measured by SEM and the chemical composition was analyzed by EDX. To the best of our knowledge, these are the first observations of the connection between the emissivity variations and the surface composition changes of SS304 during the oxidization process. Measurements of SS304 indicated that the apparent emissivity of oxidized samples showed complex behaviors determined by many factors. In future research, we shall extend the temperature and the wavelength range of our instrument and we shall add the capability to use additional types of gases, allowing us to measure materials under a more complex atmosphere.

REFERENCES

[1] A. Atkinson *et al.*, “Advanced anodes for high-temperature fuel cells,” *Nature Mater.*, vol. 3, no. 1, pp. 17–27, 2004.

[2] P. J. Ennis and W. J. Quadakkers, “Implications of steam oxidation for the service life of high-strength martensitic steel components in high-temperature plant,” *Int. J. Pressure Vessels Piping*, vol. 84, nos. 1–2, pp. 82–87, 2007.

[3] S. Grassini, M. Parvis, and A. A. Barresi, “Inert thermocouple with nanometric thickness for lyophilization monitoring,” *IEEE Trans. Instrum. Meas.*, vol. 62, no. 5, pp. 1276–1283, May 2013.

[4] R. Usamentiaga, J. Molleda, D. F. Garcia, J. C. Granda, and J. L. Rendueles, “Temperature measurement of molten pig iron with slag characterization and detection using infrared computer vision,” *IEEE Trans. Instrum. Meas.*, vol. 61, no. 5, pp. 1149–1159, May 2012.

[5] S. Westermann, T. I. Østby, K. Gisnås, T. V. Schuler, and B. Etzelmüller, “A ground temperature map of the North Atlantic permafrost region based on remote sensing and reanalysis data,” *Cryosphere*, vol. 9, no. 3, pp. 1303–1319, 2015.

[6] T. Aujeszky, G. Korres, and M. Eid, “Measurement-based thermal modeling using laser thermography,” *IEEE Trans. Instrum. Meas.*, vol. 67, no. 6, pp. 1359–1369, Jun. 2018.

[7] J. R. Howell, and R. Siegel, *Thermal Radiation Heat Transfer*, 3rd ed. New York, NY, USA: Hemisphere, 1992.

[8] T. Echaniz, R. B. Perez-Saez, and M. J. Tello, “IR radiometer sensitivity and accuracy improvement by eliminating spurious radiation for emissivity measurements on highly specular samples in the 2-25 μm spectral range,” *Measurement*, vol. 110, pp. 22–26, Jun. 2017.

[9] O. Riou, V. Guiheneuf, F. Delaleux, P.-O. Logerais, and J.-F. Durastanti, “Accurate methods for single-band apparent emissivity measurement of opaque materials,” *Measurement*, vol. 89, pp. 239–251, Jul. 2016.

[10] J. R. Markham, P. R. Solomon, and P. E. Best, “An FT-IR based instrument for measuring spectral emittance of material at high temperature,” *Rev. Sci. Instrum.*, vol. 61, no. 12, pp. 3700–3708, 1990.

[11] L. Hanssen, “Integrating-sphere system and method for absolute measurement of transmittance, reflectance, and absorptance of specular samples,” *Appl. Opt.*, vol. 40, no. 19, pp. 3196–3204, 2001.

[12] P. Honnerová, J. Martan, Z. Veselý, and M. Honner, “Method for emissivity measurement of semitransparent coatings at ambient temperature,” *Sci. Rep.*, vol. 7, no. 1, May 2017, Art. no. 1386.

[13] D. T. Vader, R. Viskanta, and F. P. Incropera, “Design and testing of a high-temperature emissometer for porous and particulate dielectrics,” *Rev. Sci. Instrum.*, vol. 57, no. 1, pp. 87–93, 1986.

[14] M. J. Ballico and T. P. Jones, “Novel experimental technique for measuring high-temperature spectral emissivities,” *Appl. Spectrosc.*, vol. 49, no. 13, pp. 335–340, 1995.

[15] P. Coppa and A. Consorti, “Normal emissivity of samples surrounded by surfaces at diverse temperatures,” *Measurement*, vol. 38, no. 2, pp. 124–131, 2005.

[16] R. Brandt, C. Bird, and G. Neuer, “Emissivity reference paints for high temperature applications,” *Measurement*, vol. 41, no. 7, pp. 731–736, 2008.

[17] R. M. Sova, M. J. Linevsky, M. E. Thomas, and F. F. Mark, “High-temperature infrared properties of sapphire, AlON, fused silica, yttria, and spinel,” *Infr. Phys. Technol.*, vol. 39, pp. 251–261, Jun. 1998.

[18] O. Rozenbaum, D. De Sousa Meneses, Y. Auger, S. Chermanne, and P. Echegut, “A spectroscopic method to measure the spectral emissivity of semi-transparent materials up to high temperature,” *Rev. Sci. Instrum.*, vol. 70, no. 10, pp. 4020–4025, Jul. 1999.

[19] S. Krenek, D. Gilbers, K. Anhalt, D. R. Taubert, and J. Hollandt, “A dynamic method to measure emissivity at high temperatures,” *Int. J. Thermophys.*, vol. 36, no. 8, pp. 1713–1725, 2015.

[20] C.-D. Wen and I. Mudawar, “Emissivity characteristics of roughened aluminum alloy surfaces and assessment of multispectral radiation thermometry (MRT) emissivity models,” *Int. J. Heat Mass Transf.*, vol. 47, nos. 17–18, pp. 3591–3605, 2004.

[21] C.-D. Wen and I. Mudawar, “Emissivity characteristics of polished aluminum alloy surfaces and assessment of multispectral radiation thermometry (MRT) emissivity models,” *Int. J. Heat Mass Transf.*, vol. 48, no. 7, pp. 1316–1329, 2005.

[22] C.-D. Wen and I. Mudawar, “Modeling the effects of surface roughness on the emissivity of aluminum alloys,” *Int. J. Heat Mass Transf.*, vol. 49, nos. 23–24, pp. 4279–4289, 2006.

[23] L. del Campo, R. B. Pérez-Sáez, and M. J. Tello, “Iron oxidation kinetics study by using infrared spectral emissivity measurements below 570 °C,” *Corrosion Sci.*, vol. 50, no. 1, pp. 194–199, 2008.

[24] D. Shi, F. Zou, S. Wang, Z. Zhu, and J. Sun, “Effect of surface oxidization on the spectral emissivity of steel 304 at the elevated temperature in air,” *Infr. Phys. Technol.*, vol. 66, pp. 6–12, Sep. 2014.

[25] D. Shi, F. Zou, Z. Zhu, and J. Sun, “Modeling the effect of surface oxidation on the normal spectral emissivity of steel 316L at 1.5 μm over the temperatures ranging from 800 to 1100 K in air,” *Infr. Phys. Technol.*, vol. 71, pp. 370–377, Jul. 2015.

[26] G. Goett, R. Kozakov, D. Uhrlandt, H. Schoepp, and A. Sperl, “Emissivity and temperature determination on steel above the melting point,” *Weld. World*, vol. 57, no. 4, pp. 595–602, 2013.

[27] P. Wang, Z. Hu, Z. Xie, and M. Yan, “A new experimental apparatus for emissivity measurements of steel and the application of multi-wavelength thermometry to continuous casting billets,” *Rev. Sci. Instrum.*, vol. 89, no. 5, 2018, Art. no. 054903.

[28] A. Mazikowski and K. Chrzanowski, “Non-contact multiband method for emissivity measurement,” *Infr. Phys. Technol.*, vol. 44, no. 2, pp. 91–99, Apr. 2003.

[29] J. Taylor. (2010). Foundation Level Infrared Training. Land Instruments International. [Online]. Available: https://www.isa.org/WorkArea/DownloadAsset.aspx?id=136908

[30] T. Echániz, I. Setién-Fernández, R. B. Pérez-Sáez, C. Prieto, R. E. Galindo, and M. J. Tello, “Importance of the spectral emissivity measurements at working temperature to determine the efficiency of a solar selective coating,” *Solar Energy Mater. Solar Cells*, vol. 140, pp. 249–252, Sep. 2015.

[31] B. Cheng, S. Price, J. Lydon, K. Cooper, and K. Chou, “On process temperature in powder-bed electron beam additive manufacturing: Model development and validation,” *J. Manuf. Sci. Eng.*, vol. 136, no. 6, 2014, Art. no. 061018.

[32] P. B. Coates, “Wavelength specification in optical and photoelectric pyrometry,” *Metrologia*, vol. 13, no. 1, pp. 1–5, 1977.

[33] A. Gouffé, “Temperature corrections of artificial black bodies, taking multiple internal diffusion into consideration,” *Rev. Opt.*, vol. 24, p. 1, 1945.

[34] H. W. Yoon, D. W. Allen, and R. D. Saunders, “Methods to reduce the size-of-source effect in radiometers,” *Metrologia*, vol. 42, no. 2, pp. 89–96, 2005.

[35] L. del Campo, R. B. Pérez-Sáez, L. González-Fernández, and M. J. Tello, “Combined standard uncertainty in direct emissivity measurements,” *J. Appl. Phys.*, vol. 107, no. 11, 2010, Art. no. 113510.

[36] *Guide to the Expression of Uncertainty in Measurement (GUM)*, Int. Org. Standardisation, Geneva, Switzerland, 1995.

[37] P. Saunders *et al.*, “Uncertainty budgets for calibration of radiation thermometers below the silver point,” *Int. J. Thermophys.*, vol. 29, no. 3, pp. 1066–1083, 2008.

[38] J. Fischer *et al.*, *Uncertainty Budgets for Realisation of Scales by Radiation Thermometry*, BIPM Document CCT/03-03, 2003. [Online]. Available: https://www.bipm.org/cc/CCT/Allowed/22/CCT03-03.pdf

[39] T. P. Jones and J. Tapping, “A precision photoelectric pyrometer for the realization of the IPTS-68 above 1064.43 °C,” *Metrologia*, vol. 18, no. 1, pp. 23–31, 1982.

[40] T. Ricolfi and L. Wang, “Experiments and remarks on the size-of-source effect in precision radiation thermometry,” in *Proc. TEMPMEKO*, vol. 93, 1993, pp. 161–165.

[41] P. Saunders and H. Edgar, “On the characterization and correction of the size-of-source effect in radiation thermometers,” *Metrologia*, vol. 46, no. 1, pp. 62–74, 2009.

[42] G. Machin and M. Ibrahim, “Size of source effect and temperature uncertainty II: Low temperature systems,” in *Proc. TEMPMEKO*, vol. 99, Sep. 1999, pp. 687–692.

[43] J. G. Harris and Y.-M. Chiang, “Nonuniformity correction of infrared image sequences using the constant-statistics constraint,” *IEEE Trans. Image Process.*, vol. 8, no. 8, pp. 1148–1151, Aug. 1999.

[44] P. Saunders, *Radiation Thermometry: Fundamentals and Applications in the Petrochemical Industry*. Bellingham, WA, USA: SPIE, 2007.

[45] Y. F. Liu, Z. L. Hu, D. H. Shi, and K. Yu, “Experimental investigation of emissivity of steel,” *Int. J. Thermophys.*, vol. 34, no. 3, pp. 496–506, 2013.

[46] S. H. Ham, C. Carteret, J. Angulo, and G. Fricout, “Relation between emissivity evolution during annealing and selective oxidation of TRIP steel,” *Corrosion Sci.*, vol. 132, pp. 185–193, Mar. 2018.

[47] J. C. Langevoort, I. Sutherland, L. J. Hanekamp, and P. J. Gellings, “On the oxide formation on stainless steels AISI 304 and incoloy 800H investigated with XPS,” *Appl. Surf. Sci.*, vol. 28, no. 2, pp. 167–179, 1987.

[48] A. M. Huntz *et al.*, “Oxidation of AISI 304 and AISI 439 stainless steels,” *Mater. Sci. Eng., A*, vol. 447, nos. 1–2, pp. 266–276, 2007.

[49] I. Saeki *et al.*, “Growth process of protective oxides formed on type 304 and 430 stainless steels at 1273 k,” *Corrosion Sci.*, vol. 40, no. 8, pp. 1295–1302, 1998.

[50] R. Guillamet, J. Lopitaux, B. Hannoyer, and M. Lenglet, “Oxidation of stainless steels (AISI 304 and 316) at high temperature. Influence on the metallic substratum,” *Le J. de Phys.*, vol. 3, no. C9, pp. C9-349–C9-356, 1993.

[51] J.-H. Kim, D.-I. Kim, S. Suwas, E. Fleury, and K.-W. Yi, “Grain-size effects on the high-temperature oxidation of modified 304 austenitic stainless steel,” *Oxidation Met.*, vol. 79, nos. 3–4, pp. 239–247, 2012.

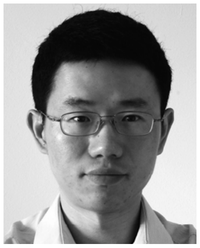

Chengxi Zhu received the B.Eng. degree in mechanical engineering from Donghua University, Shanghai, China, in 2006, and the M.S. degree in optical engineering from the University of Chinese Academy of Sciences, Shanghai, in 2014. He is currently pursuing the Ph.D. degree with the University of Sheffield, Sheffield, U.K.

His current research interests include the emissivity measurement, infrared radiation temperature measurement, and optical and mechanical engineering in applications of advanced thermal imaging technology.

Matthew J. Hobbs received the M.Eng. and Ph.D. degrees from the Department of Electronic and Electrical Engineering, University of Sheffield, Sheffield, U.K., in 2009 and 2014, respectively.

From 2013 to 2016, he was a Knowledge Transfer Associate with Land Instrument International Ltd., Dronfield, U.K., in collaboration with the University of Sheffield. He has been a Research Associate with the University of Sheffield. His current research interests include design, optimization, and evaluation of novel instrumentation for noncontact infrared temperature measurements and thermal imaging, and the application of novel and commercial infrared photodetector technology within such instrumentation.

Robert C. Masters received the M.Phys. degree in physics and astronomy from the University of Sheffield, Sheffield, U.K., in 2013, and the Ph.D. degree from the Department of Materials Science and Engineering, University of Sheffield, in 2018.

He is currently a Research Associate with the University of Sheffield. His current research interests include characterizing the morphology and performance of organic electronic materials, using advanced electron microscopy techniques as a tool to understand material properties on the nanoscale.

Cornelia Rodenburg received the Ph.D. degree from Sheffield Hallam University, Sheffield, U.K., in 2001.

She was a Post-Doctoral Research Associate with the University of Cambridge, Cambridge, U.K. She is currently a Senior Lecturer with the Materials Science and Engineering Department, University of Sheffield. To gain novel insights on complex phenomena involving both, structural and chemical changes on the nano-scale, her group is pioneering novel spectroscopy and imaging methods in scanning charged particle microscopes. Her current research interest includes a wide range of materials from natural soft materials to hard ceramic coatings and steels.

Jon R. Willmott received the Ph.D. degree from the University of Southampton, Southampton, U.K., in 2003.

From 2002 to 2004, he was a Post-Doctoral Research Associate of molecular materials with the University of Cambridge, Cambridge, U.K. From 2004 to 2015, he was a Physicist with Land Instruments International Ltd., Dronfield, U.K. He is currently a Senior Lecturer of sensors systems with the University of Sheffield, Sheffield, U.K. He is an expert in radiation thermometry, thermal imaging, optical design, instrumentation, and radiometry.